Supporting Information

A Tribenzocoronene-Based 2D Conductive Metal-Organic Framework for Efficient Energy Storage

Jing Zhao,[a] Ting Zhang,[a] Junyu Ren,[b] Ziqiang Zhao,[a] Xi Su,[a] Weihua Chen,*[c] Long Chen*[a,b]

[a]Department of Chemistry, Tianjin Key Laboratory of Molecular Optoelectronic Science, Tianjin University, Tianjin 300072, China

[b]State Key Laboratory of Supramolecular Structure and Materials, College of Chemistry, Jilin University, Changchun 130012, China

[c]College of Chemistry and Green Catalysis Center, Zhengzhou University, Henan 450001, China

E-mail: chenweih@zzu.edu.cn; long.chen@tju.edu.cn

Table of Contents

Section 1. Materials and Methods

Iron (III) chloride, 1,2-dimethoxybenzene, dibromine, potassium carbonate, tetrakis(triphenylphosphine)palladium (0), phenylboronic acid, and tribromoborane were purchased from commercial sources. All organic solvents including acetone, tetrahydrofuran (THF), *N,N*-dimethylacetamide (DMAc) and methanol (MeOH) were analytical grade reagents and used without further purification.

General characterization: Solution ^{1}H nuclear magnetic resonance (NMR) spectra of all organic compounds were recorded on a Bruker AVANCE III-400 NMR spectrometer. MALDI-TOF spectrometry measurements were performed on the Bruker Autoflex Speed TOF/TOF mass spectrometer. Fourier transform infrared (FT-IR) spectra were recorded in reflection mode on a Bruker Alpha spectrometer in the range of 400-4000 cm^{-1}. X-ray photoelectron spectroscopy (XPS) was carried out on Thermo Scientific K-Alpha using 0.6 eV Al Kα radiation. The base pressure was about 3×10^{-7} mbar. The binding energies were referenced to the C_{1s} line at 284.8 eV from adventitious carbon. Elemental analysis (C, H) was performed on a PerkinElmer 240C elemental analyzer. The Cu contents in Cu-TBC was determined by ICP-MS technique using Agilent 725ES & Agilent 5110. The powder X-ray diffraction patterns were recorded on X-ray diffractometer RIGAKU SMARTLAB9KW or DX-27mini X-Ray diffractometer with a Cu-target tube and a graphite monochromator. Field emission scanning electron microscopies were carried out using a Hitachi Limited model SU8010 microscope operating at an accelerating voltage of 5.0 kV. Transmission electron microscopies were conducted on a FEI model Tecani 20 microscope and a JEOL model JSM-2100F. The simulations of the possible structures were carried out in Accelrys Material Studio 8.0 software package. The simulated PXRD patterns were determined by the Reflex module. Pawley refinements of the experimental PXRD of Cu-TBC were conducted to optimize the lattice parameters iteratively until the R_{wp} value converges. The porosities of MOF were measured by N_2 adsorption and desorption at 77 K using a Bel Japan Inc. model BELSOPR-max analyzer and the samples were degassed at 80 °C for 10 h under vacuum (10^{-5} bar) before analysis. The pore size distribution was calculated from the adsorption branch by nonlocal density functional theory (NLDFT) method. The thermal stability of MOF was evaluated on a thermogravimetric analysis (TGA) with a differential thermal analysis instrument (TA Instruments TGA Q50-1918 analyzer) over the temperature range from 35 to 800 °C in flowing N_2 with a heating

rate of 10 °C min^{-1} using an empty Al_2O_3 crucible as the reference. All electrochemical measurements were carried out using a CHI 760E electrochemical workstation (CH Instruments, Chenhua Co., Shanghai, China).

Calculation Methods:

The Cu-TBC samples for Cyclic voltammetry (CV) measurements are treated as follows:

Cu-TBC (60 wt%), carbon black (30 wt%), and Nafion binder (10 wt%) were dispeased into ethanol. The mixture was droped onto a glassy carbon (GC) electrode and dried under room temperature, which was subjected in 0.1 M H_2SO_4 electrolyte for CV tests.

Gravimetric capacitances in three electrodes systems are calculated from GCD profiles according to equation (1):

$$C = \frac{I_g \times \Delta t}{\Delta U} \tag{1}$$

Where C (F g^{-1}) is the gravimetric capacitance, I_g (A g^{-1}) stands for the current density, Δt (s) is the discharge time, and ΔU (V) is the potential window interval.

Calculation for Energy Density (E) and Power Density (P):

Capacitance of the two electrodes devices is calculated using the follow equations:

$$C = \frac{I \times \Delta t}{\Delta U \times m} \tag{2}$$

Where C (F g^{-1}) is the gravimetric capacitance of the Cu-TBC // AC device. I (A) is the charge-discharge current, Δt (s) represents the discharge time, ΔU (V) corresponds to the voltage change. m (g) is the total mass of active material.

The gravimetric energy density (E) and power density (P) are calculated according to the following two equations:

$$E\,(W\,h\,kg^{-1}) = \frac{0.5 \times C \times \Delta U^2}{3.6} \tag{3}$$

$$P\,(kW\,kg^{-1}) = \frac{3.6 \times E}{\Delta t} \tag{4}$$

Where E (W h kg^{-1}) is the gravimetric energy density, P (kW kg^{-1}) is the gravimetric power density of the asymmetrical device, C is the gravimetric capacitances of the device, ΔU is the voltage window, Δt is the discharge time.

Capacitance Contribution Calculation Methods

Trasatti **Method**

The *Trasatti* method was used to differentiate the capacitance contribution from pseudocapacitance (C_p) and electrical double layer capacitance (C_{dl}) reactions. CV measurements of the Cu-TBC were first obtained with the scan rates ranging from 2 to 100 mV s^{-1}. Then, corresponding gravimetric capacitances were evaluated based on aforesaid equation (1).

Plotting the reciprocal of gravimetric capacitances (C^{-1}) against the square root of scan rates ($v^{0.5}$) should yield a linear correlation between them (Fig. 3b). Specifically, the correlation can be described by the following equation (5):

$$C^{-1} = constant \; v^{0.5} + C_T^{-1} \tag{5}$$

Where C is experimental gravimetric capacitance, v is the scan rate and C_T is the total capacitance, respectively. The "total capacitance" equals the sum of electrical double layer capacitance and pseudocapacitance.

Plotting the gravimetric capacitances (C) against the reciprocal of square root of scan rates ($v^{-0.5}$) should also give a linear correlation described by the following equation (6) (if assuming a semi-infinite diffusion of ions): (Fig. 3a)

$$C = constant \; v^{-0.5} + C_{dl} \tag{6}$$

Linear fit the plot and extrapolate the fitting line to y-axis gives the maximum electrical double layer capacitance (C_{dl}). Subtraction of C_{dl} from C_T got the maximum C_p.

Dunn **Method**

The *Dunn* method was applied to quantitatively differentiate the capacitance contribution from surface capacitive effects (regarded as pseudocapacitance reactions) and diffusion-controlled processes capacitive effects (regarded as electrical double layer capacitance effects). At a fixed potential, the current density [$I_{(V)}$] read from a CV can be expressed as a combination of two terms as follow:

$$I_{(V)} = k_1 v + k_2 v^{0.5} \tag{7}$$

Where the term $k_1 v$ accounts for the current density contributed from surface capacitive effects, while the term $k_2 v^{0.5}$ is the current density associated with diffusion-controlled processes. Dividing $v^{0.5}$ on both sides of the equation (7) yields:

$$I_{(V)}/v^{0.5} = k_1 v^{0.5} + k_2 \tag{8}$$

Therefore, image of $I_{(V)}/v^{0.5}$ vs. $v^{0.5}$ was plotted by fetching the $I_{(V)}$ from CVs obtained under a series of scan rates, where a linear fitting line was obtained with slope equals k_1 and y-intercept of k_2. Plugging the obtained k_1 and k_2 into equation (7) allowed one to differentiate the capacitance contribution from diffusion-controlled processes and surface capacitive effects at the specific potential V and a selected scan rate v. The capacitance ratio of surface capacitive effects to diffusion-controlled processes equals the ratio of the area of the pink region to the area of the blue region (Fig. 3c).
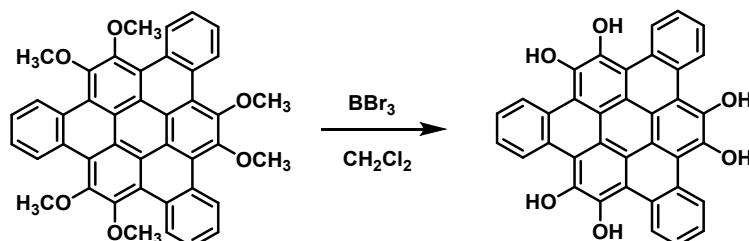
Repeating the aforementioned steps for other scan rates results in the capacitance ratio of diffusion-controlled processes and surface capacitive effects illustrated by Fig. 3d.

Section 2. Synthetic Procedures

Synthesis of 6OCH$_3$-TBC-

6OCH$_3$-TBC was synthesized according to the literature[S1].

Synthesis of 6OH-TBC

Scheme S1. Synthesis of 6OH-TBC.

Under a nitrogen atmosphere, 6OCH$_3$-TBC (200 mg, 0.37 mmol) was dissolved in dry CH$_2$Cl$_2$ (20 mL), and then BBr$_3$ (2 mmol) was added gently at 0 °C. The mixture was stirred at room temperature. After stirring for 12 hours, the reaction mixture was quenched with distilled water. The solid was collected by filtration and washed with water to give a yellow-green solid 6OH-TBC. Yield: 135 mg, 55.6%. ^{1}H NMR (400 MHz, DMSO-d_6): δ (ppm) 10.21 (dd, 6H), 7.79 (dd, 6H); MALDI-TOF: m/z (C$_{36}$H$_{18}$O$_6$) calculated for [M+Na$^+$] 569.1, found 570.1. The ^{13}C NMR spectrum of 6OH-TBC was not obtained due to its low solubility.
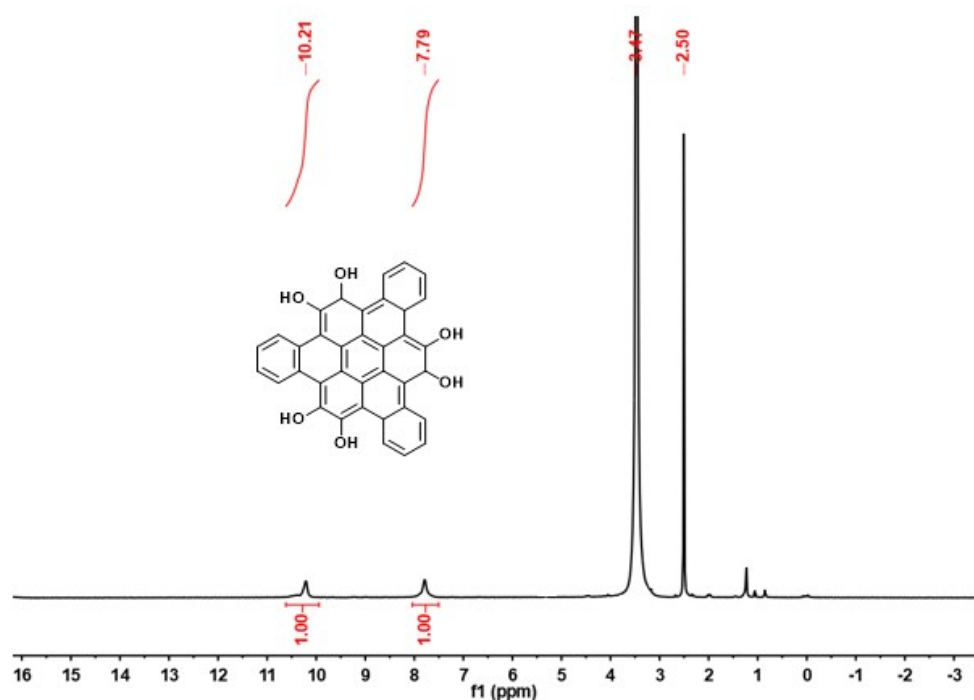
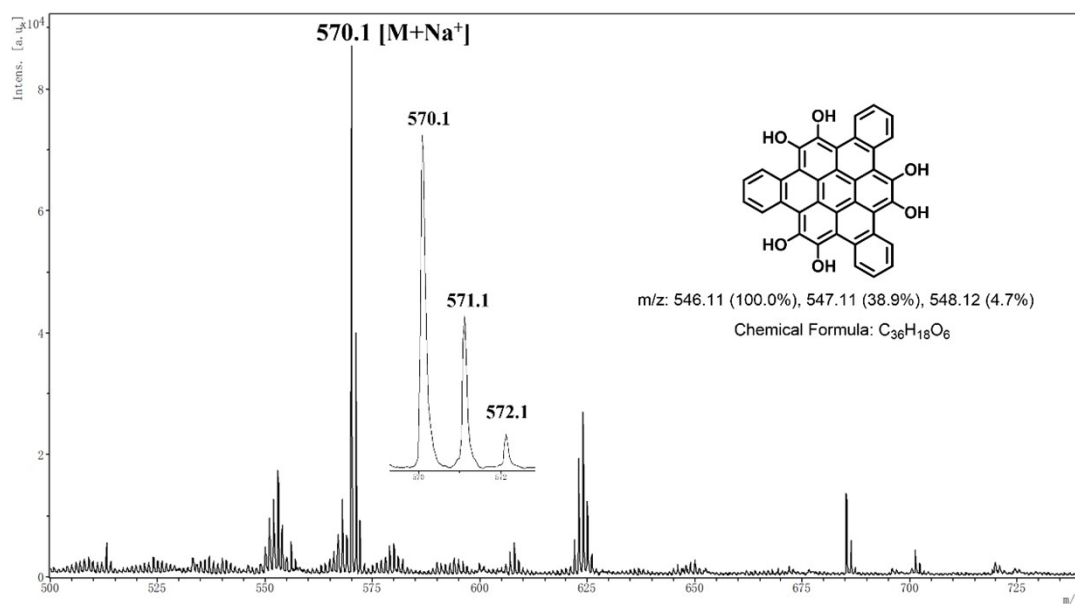**Fig. S1.** ^{1}H NMR spectrum of 6OH-TBC in DMSO-d_6.

Fig. S2. MALDI-TOF mass spectrum of 6OH-TBC.

Preparation of Cu-TBC

6OH-TBC ligand (11.0 mg, 0.02 mmol) and bis(1,1,1-trifluoropentane-2,4-dionato-O,O')copper (29.5 mg, 0.08 mmol) were dissolved in a mixed solution of DMAc, MeOH and water (0.5 mL/1 mL/1mL) in a Pyrex tube (10 mL). The tube was then heated at 120 °C for three days. After cooling, the precipitate was filtered and thoroughly washed with DMAc, MeOH and acetone, and dried under vacuum to afford Cu-TBC as a black powder (8.9 mg, 70.0%). Elemental analysis (EA) and inductively coupled plasma emission spectroscopy (ICP) (wt.%) calcd. for: $\{C_{72}H_{24}Cu_3O_{12}\}_n$: C, 68.01; H, 1.90; Cu, 14.99%. Found: C, 69.86; H, 2.85; Cu: 14.20%.

Section 3. Electrochemical Measurements

Standard three-electrode system measurements

The three-electrode measurements were carried out using Ag/AgCl as the reference electrode, platinum wire as the counter electrode, and Cu-TBC modified glassy carbon electrode (GCE) with an area of 0.07 cm^2 as the working electrode. The MOF slurry was prepared by ultrasonically mixing the as-prepared MOF powder (6.0 mg), conductive carbon black (3.0 mg), 23.0 µL Nafion (5 wt%, dispersed in water) and dry ethanol (577.0 µL) for 30 min to form a homogeneous suspension. 8 µL of well-dispersed MOF slurry was pipetted and spread onto the surface of a pre-polished GCE, thereafter dried in air for 1 h before measurement, corresponding to MOF loading of 1.14 mg cm^{-2}. CV curves were recorded in the potential range of -0.4 to 0.6 V (vs Ag/AgCl) at various scan rates ranging from 2 to 100 mV s^{-1}. Galvanostatic charge-discharge (GCD) tests were performed at current densities from 0.2 to 20.0 A g^{-1}. The gravimetric capacitance (C_g) of the Cu-TBC were calculated based on the discharge curves. Electrochemical impedance spectroscopy (EIS) measurements were carried out from 10 mHz to 1 MHz at bias voltages.

Preparation of the MOF and AC film electrode

To prepare the MOF based electrode, MOF powder (12.0 mg), conductive carbon black (6.0 mg), and Nafion binder solution (46 µL, 5 wt%, dispersed in water) were added to dry ethanol (1.15 mL). The mixture was stirred for 30 min to form a homogeneous suspension. 60 µL of well-dispersed MOF slurry was pipetted and spread onto the surface of a pre-polished round titanium mesh electrode (r = 0.6 cm). The resulting Cu-TBC based electrode was dried at 80 °C under vacuum overnight. The Cu-TBC based electrode was composed of 60 wt% MOF, 30 wt% conductive carbon black and 10 wt% Nafion.

The active carbon (AC) based electrode was prepared via the same method as Cu-TBC based electrode using only AC (24 mg) and Nafion binder (92 µL).

Preparation of Two-electrode Asymmetrical MOF//AC device

To build the two-electrode asymmetrical MOF//AC device, a Cu-TBC loaded round titanium mesh (active mass ≈ 0.53 mg cm^{-2}) was used as anode and an AC loaded

round titanium mesh (active mass $\approx$ 5.3 mg cm^{-2}) was used as cathode Meanwhile, an NKK-MPF30AC-100 membrane and 50 μL 0.1 M H$_2$SO$_4$ aqueous solution were used as separator and electrolyte, respectively.
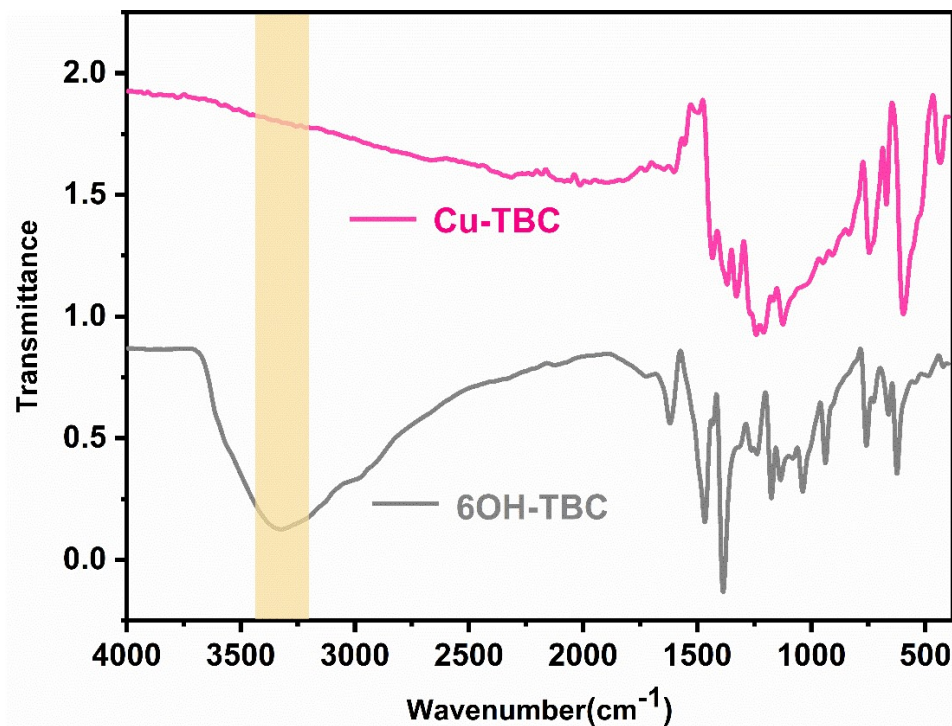
Section 4. FT-IR Spectra

Fig. S3. The comparison of the FT-IR spectra of Cu-TBC and 6OH-TBC.

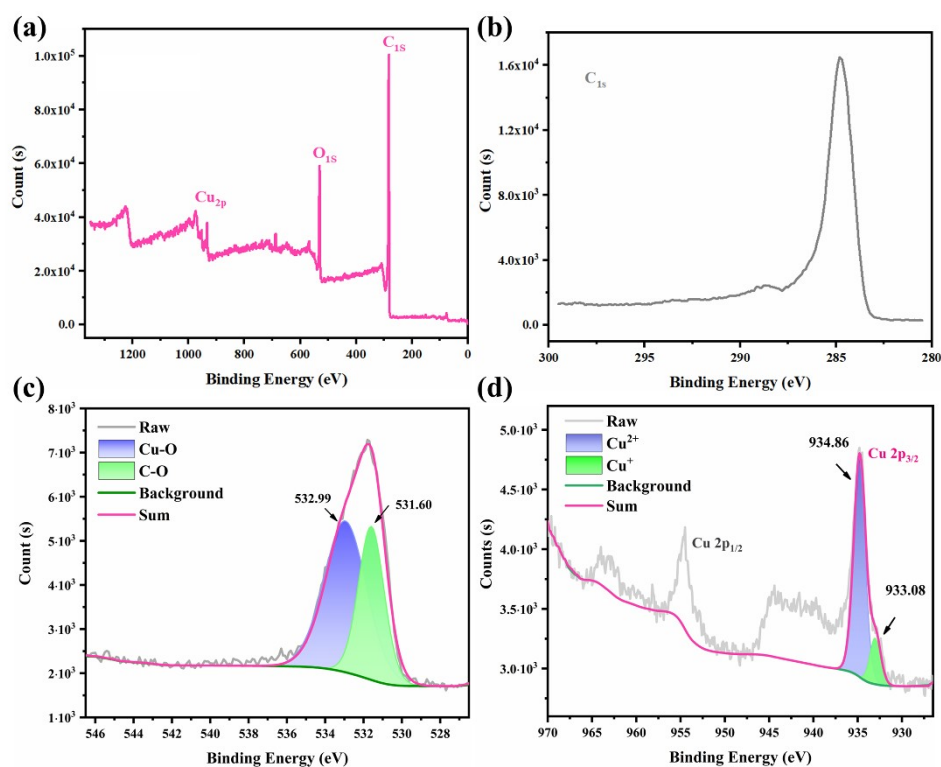# Section 5. X-Ray Photoelectron Spectroscopy Analysis

Fig. S4. (a) XPS analysis of full energy spectrum for all the elements of Cu-TBC. (b) Zoomed-in spectrum of C (1s). (c) Zoomed-in spectrum of O (1s). (d) Zoomed-in spectrum of Cu (2p).

Table S1. Area and FWHM of deconvoluted peaks of the Cu ($2p_{2/3}$) region in the XPS of Cu-TBC.

Band	Position (eV)	FWHM	Area (%)
Cu ($2p_{2/3}$)-1	934.86	2.64	96.81
Cu ($2p_{2/3}$)-2	933.08	1.45	3.19

Table S2. Area and FWHM of deconvoluted peaks of the O (1s) region in the XPS of Cu-TBC.

Band	Position (eV)	FWHM	Area (%)
O (1s)-1	532.99	2.70	64.37
O (1s)-2	531.60	1.65	35.63

Section 6. Elemental Analysis and ICP-MS

Table S3. Elemental analysis of Cu-TBC.

		C (wt%)	H (wt%)
$Cu_3(6O\text{-}TBC)_2$	Calcd.	68.01	1.90
	Found	69.86	2.80

Table S4. Cu contents of Cu-TBC.

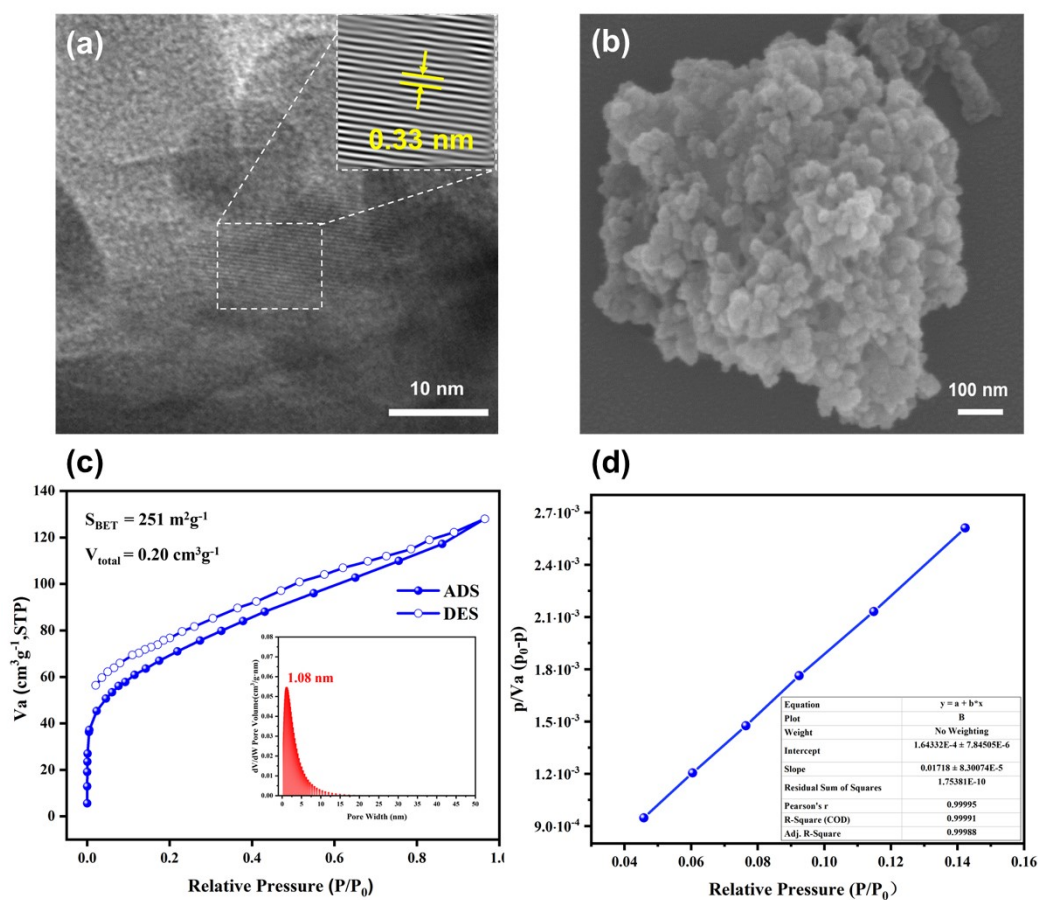|		Cu (wt%)
$Cu_3(6O\text{-}TBC)_2$	Calcd.	15.99
	Found	14.20

Fig. S5. (a) TEM and (b) SEM images of Cu-TBC. (c) The N_2 sorption isotherm for Cu-TBC. Adsorption and desorption points are represented by solid and empty circles, respectively. Inset: pore-size distribution of Cu-TBC. (d) BET plot of Cu-TBC calculated from N_2 adsorption isotherm at 77 K.
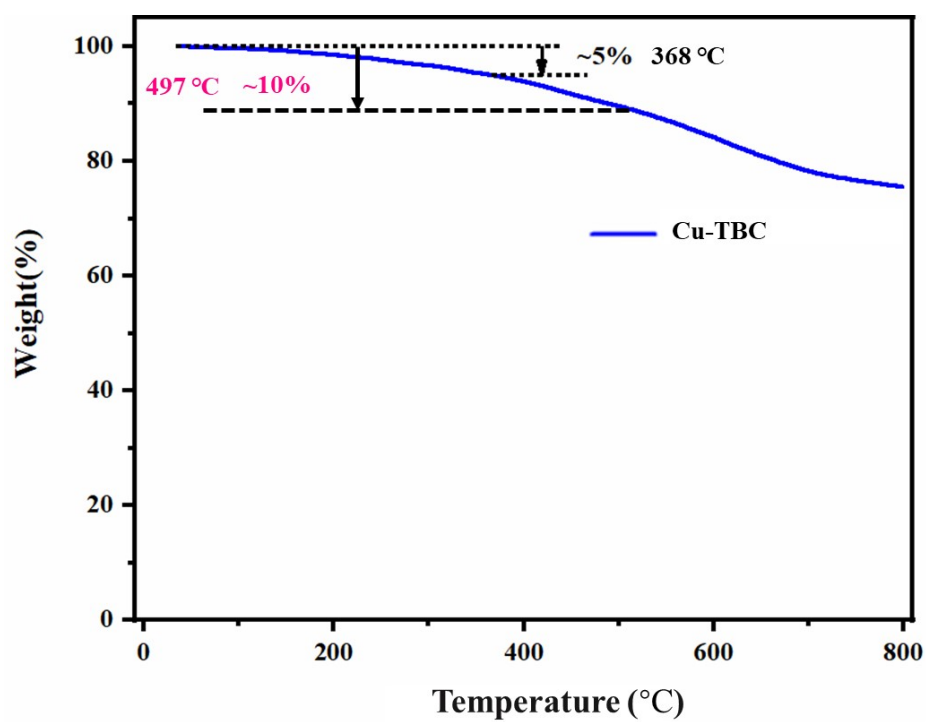
Section 8. Thermogravimetric Analysis

Fig. S6. TGA curve of Cu-TBC.
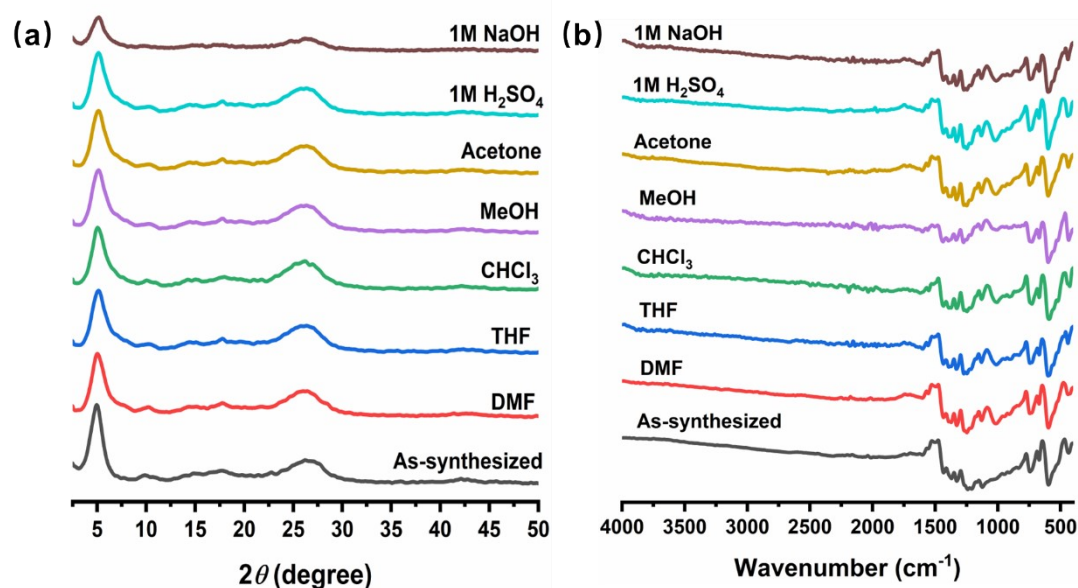
Section 9. Chemical Stability Tests

Fig. S7. (a) PXRD patterns, (b) FT-IR spectra of Cu-TBC before and after immersing in different solvents for three days.

Section 10. Electrical Conductivity Measurements

Electrical conductivity measurements were conducted with a two-probe method using a Keithley model 4200-SCS source meter. For the electrical conductivity measurements, two pieces of gold wire were attached to the side of sample and fixed by silver colloid which was contact to the source meter. The current-voltage (*I-V*) curve measurement was performed by sweeping the voltage in the range of −1.0 to 1.0 V at various temperatures.
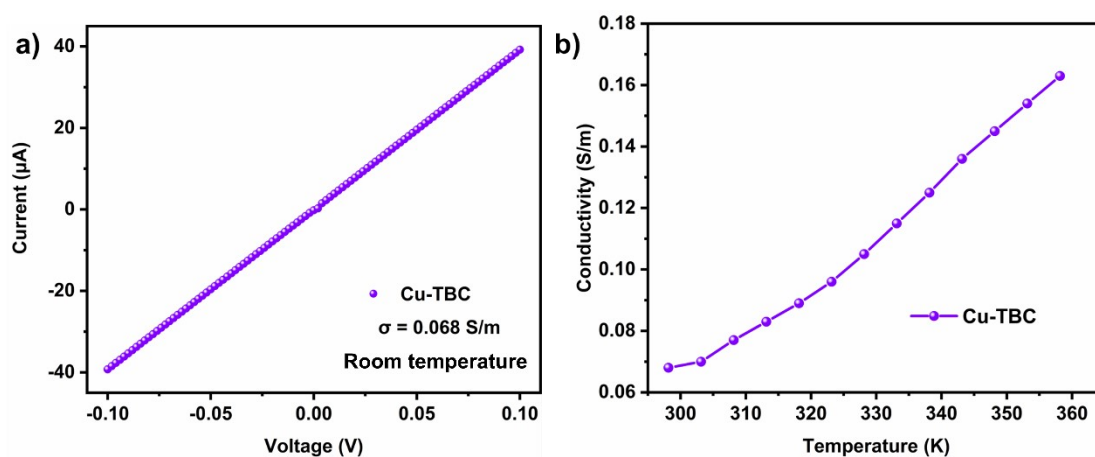

Fig. S8. (a) *I-V* curves for Cu-TBC at room temperature. (b) Temperature-dependence conductivities for Cu-TBC.

Table S5. Comparison of electrically conductivity recently 2D MOFs.

Materials	Conductivity (S cm^{-1})	Ref.
Cu-TBC	**6.8×10^{-4}** (two-probe pellet)	**This work**
Cu-HAB	0.11 (four-contact pellet)	*Nat. Energy.* **2018**, *3, 30.*
Ni-HAB	0.7 (four-contact pellet)	
Cu-HHB	7.3×10^{-8} (van der Pauw pellet)	*J. Am. Chem. Soc.* **2018**, *140, 14533.*
Cu-HHTP	0.02 (two-probe film)	*Angew. Chem., Int. Ed.* **2017**, *56, 16510.*
Ni-HHTP	0.01 ± 0.003 (two-probe pellet)	*Chem. Mater.* **2016**, *28, 5264.*
Cu-HHTQ	2.74×10^{-5} (two-probe pellet)	*Nano Res.* **2021**, *14, 369.*
Cu-HITP	0.2 (two-point probe pellet)	*Angew. Chem., Int. Ed.* **2017**, *56, 16510.*

Section 11. Electrochemical Performance in Three Electrodes System
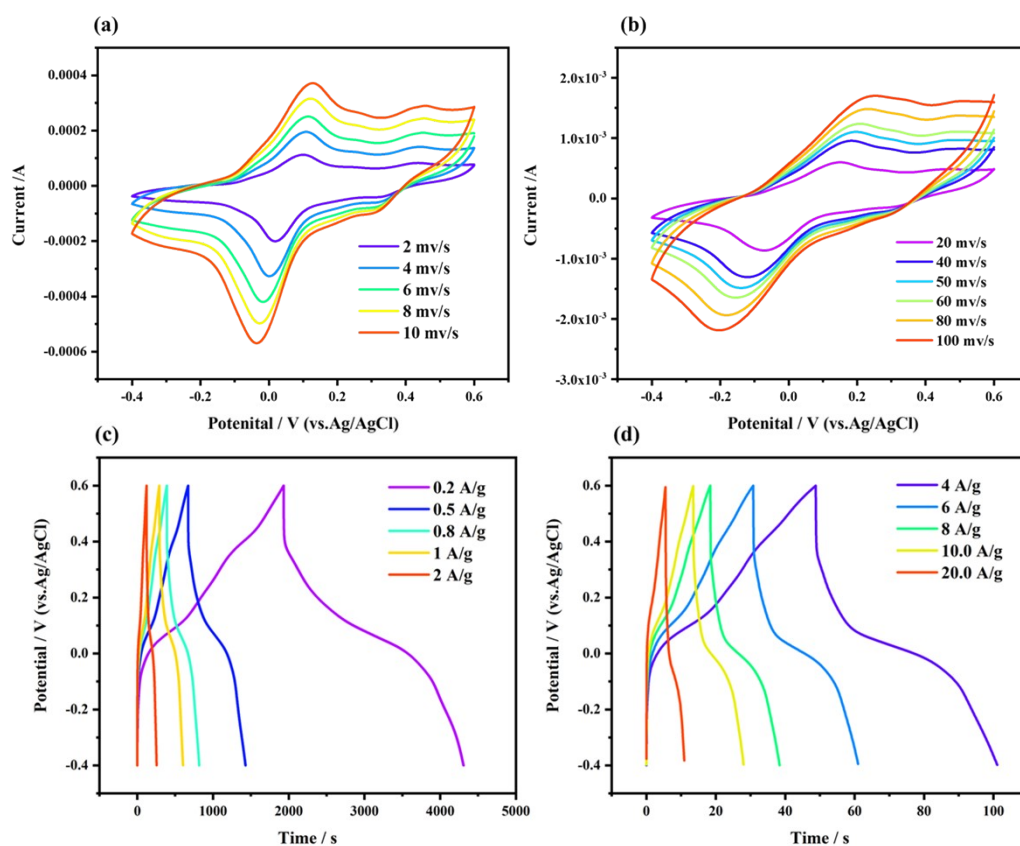
Fig. S9. (a, b) CV curves at different scan rates of Cu-TBC; (c, d) GCD curves of Cu-TBC at different current densities.

Fig. S10. Gravimetric capacitance of Cu-TBC dependence on current densities

Section 12. Electrochemical Performance of Two Electrodes Devices

Fig. S11. Schematic diagram of two-electrode asymmetrical Cu-TBC//AC device.

Fig. S12. (a, b) CV curves at different scan rates of Cu-TBC//AC; (c, d) GCD curves of Cu-TBC//AC at different current densities.

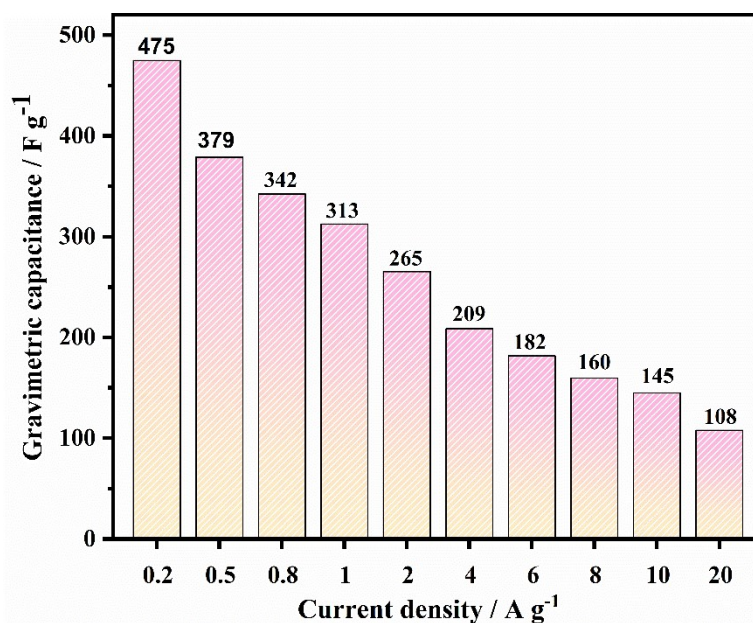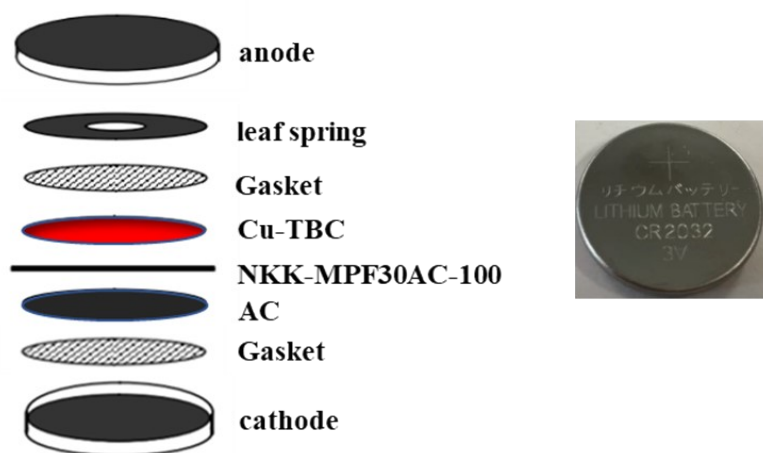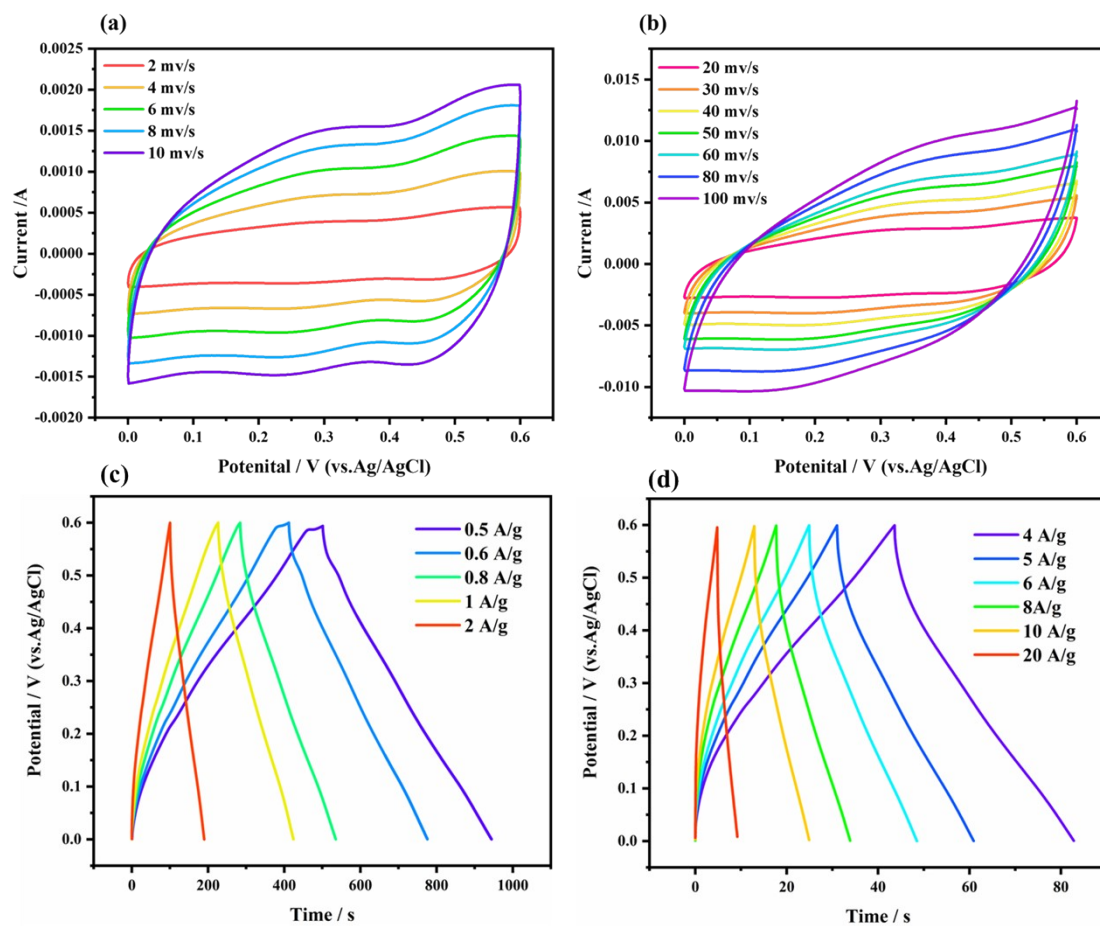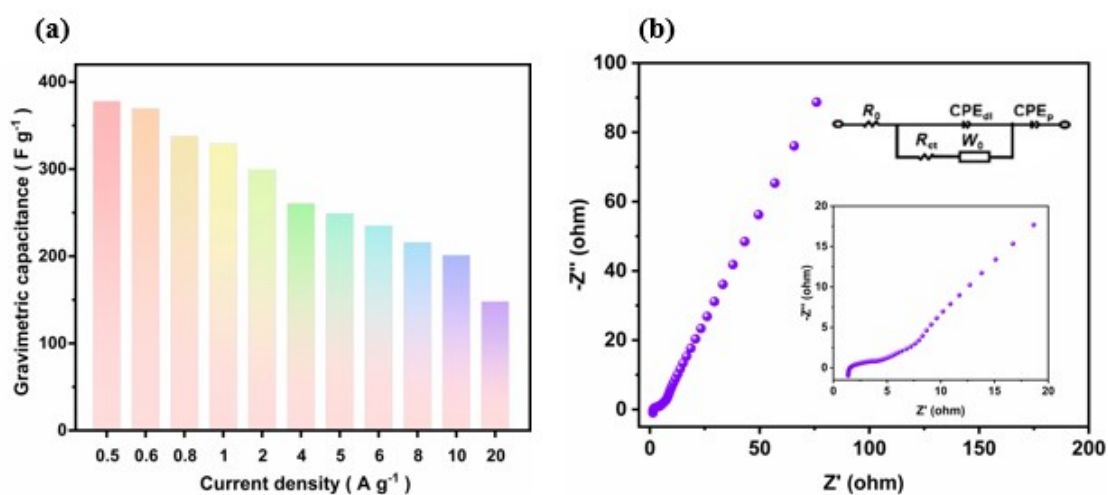**Fig. S13.** (a) the calculated capacitances and (b) The Nyquist plot of Cu-TBC//AC device. Inset: high-frequency region and the equivalent circuit of Cu-TBC electrode.

Table S6. Gravimetric capacitances, energy densities and power densities of the Cu TBC//AC device at different current densities.

Current density (A g⁻¹)	Gravimetric capacitance (F g⁻¹)	Energy density (W h kg⁻¹)	Power density (kW kg⁻¹)
0.5	377.75	18.89	0.15
0.6	369.60	18.48	0.18
0.8	337.71	16.88	0.24
1	329.32	16.46	0.3
2	299.36	14.96	0.6
4	260.67	13.03	1.2
5	249.08	12.45	1.5
6	235.13	11.75	1.8
8	215.86	10.79	2.4
10	201.16	10.06	3
20	148.02	7.40	6

Section 13. The Proposed Redox Mechanism of Cu-TBC

To explore the redox mechanism of Cu-TBC, the electrochemical performance of 6OH-TBC ligand was investigated for comparison. As shown in Fig. S14a, at a scan rate of 2 mV s^{-1}, the 6OH-TBC ligand displayed three pairs of redox peaks at 0.09/0.02 V, 0.27/0.19 V and 0.43/0.33 V (*vs*. Ag/AgCl) respectively. Compared with Cu-TBC, the gravimetric capacitance of the ligand was smaller (Fig. S14b), which may be due to poor conductivity hindering electron transfer. This speculation was further verified by EIS profiles, as shown in Fig. S14c, the equivalent ohmic resistance at the electrode/electrolyte interface of Cu-TBC was significantly lower than those of 6OH-TBC ligand. In addition, at a current density of 5 A g^{-1}, 6OH-TBC exhibited a capacitance retention of 72% after performing 2000 cycles (Fig. S14Sead), and its cycling stability was significantly inferior to that of the Cu-TBC.
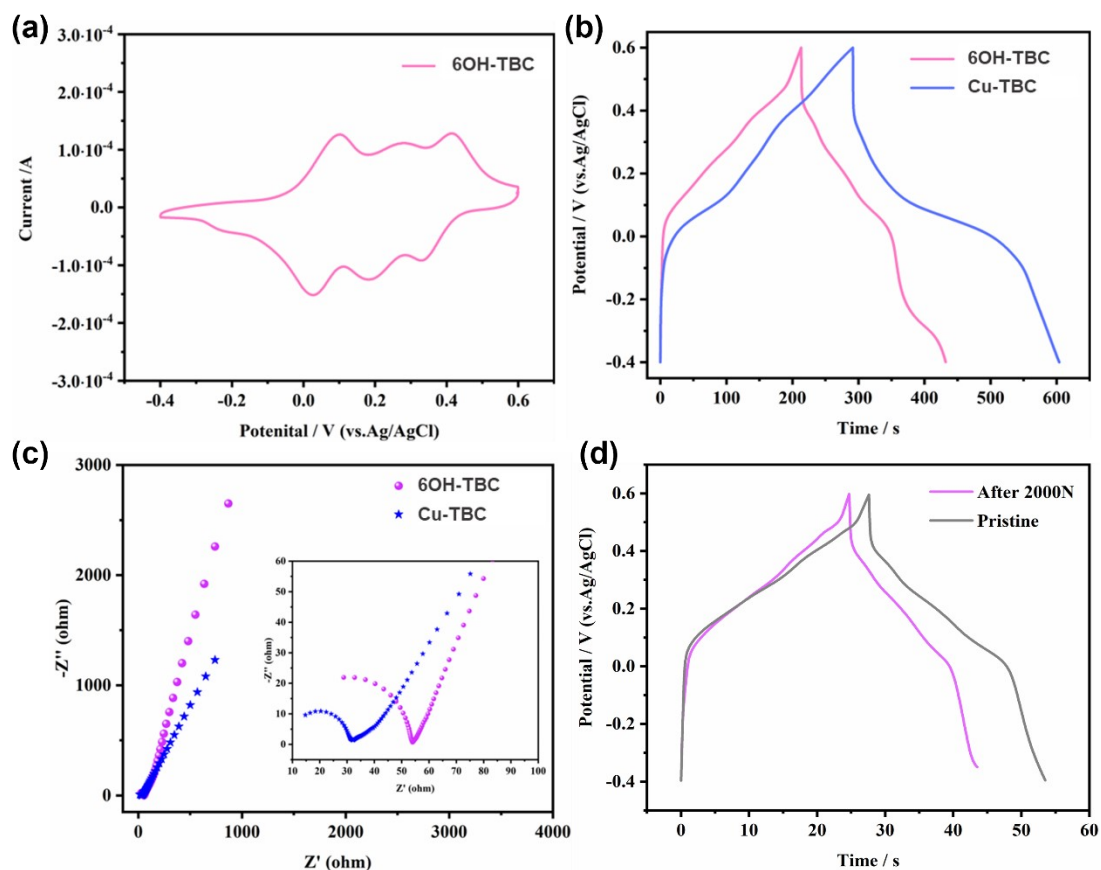

Fig. S14. (a) CV curve of 6OH-TBC at 2 mV s^{-1}. (b) GCD profiles of Cu-TBC and 6OH-TBC collected at 1.0 A g^{-1}. (c) Nyquist plot of Cu-TBC and 6OH-TBC. Inset shows the high frequency domain. (d) Comparison of galvanostatic charge-discharge curves of 6OH-TBC ligand after 2000 cycles at a current density of 5 A g^{-1}.

By comparison with the 6OH-TBC ligand, no new redox peaks were observed in the CV curve of Cu-TBC, indicating that the valence state of Cu maintained during the charge/discharge process. Therefore, it is inferred that the charge storage/release process should take place on the ligand hydroxyl group. Accordingly, the possible mechanism of the reversible redox reaction during the process was proposed as displayed in Scheme S2. Similar redox processes and mechanisms have been described in other literatures[S2-S4].
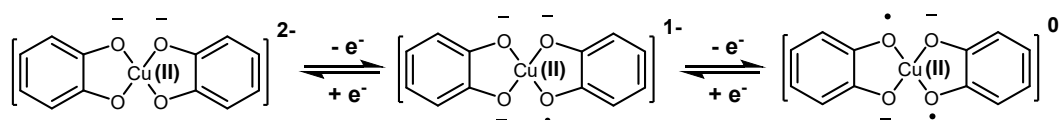
Scheme S2. The possible redox mechanism of Cu-TBC during charge/discharge process.

Section 14. Gravimetric Capacitance Comparison of Cu-TBC with Other Materials in Three Electrodes System

Table S7. Gravimetric capacitance comparison of Cu-TBC and other materials in three-electrode system.

Materials	Electrolyte	Gravimetric capacitance $(F\ g^{-1})$	Ref.
Cu-TBC	**0.1 M H_2SO_4**	**379 (0.5 A g^{-1})**	*This work*
Cu-DBC	1 M NaCl	425 (0.5 A g^{-1})	*Angew. Chem.,Int. Ed.* 2020, 59, 1081.
$Cu_3(HHTP)_2$	3 M KCl	202 (0.5 A g^{-1})	*Adv. Funct. Mater.* **2017**, 27, 1702067.
$Ni_2[CuPc(NH)_8]$	1 M Na_2SO4	400 (0.5 A g^{-1})	*J. Am. Chem. Soc.* **2021**, 143, 10168.
Cu-HAB	1 M KOH	215 (0.2 mV s^{-1})	*Nat. Energy.* **2018**, 3, 30.
Co-BDC	1 M LiOH	207 (0.6 A g^{-1})	*Microporous Mesoporous Mat.* **2012**, 153, 163.
Cu-POMOF	1 M H_2SO_4	237 (2 A g^{-1})	*Chem. Eng. J.* **2019**, 373 , 587–597.
Graphene	1 M H_2SO_4	198 (0.5 A g^{-1})	*Science* **2013**, 341, 534.
Nanoporous MXene	3 M H_2SO_4	351 (0.5 A g^{-1})	*Nanoscale* **2018**, 10, 9642.
Porous carbon	6 M KOH	280 (0.5 A g^{-1})	*Nano Energy* **2020**, 70, 104531.
Porous polymer	1 M Na_2SO_4	250 (0.5 A g^{-1})	*J. Am. Chem. Soc.* **2018**, 140, 10960.

Section 15. Performance Comparison of Cu-TBC with Other Capacitor Materials Based Solid-State Supercapacitors

Table S8. The energy density and power density of symmetric devices based solid-state supercapacitors compared with other capacitor materials.

Materials	Power density (kW kg^{-1})	Energy density (Wh kg^{-1})	Ref.
	0.15	18.89	
	0.18	18.48	
	0.24	16.88	
	0.3	16.46	
	0.6	14.96	
Cu-TBC	1.2	13.03	*This Work*
	1.5	12.45	
	1.8	11.75	
	2.4	10.79	
	3	10.06	
	6	7.40	
	0.1	13.8	
	0.25	12.7	
	0.36	12.2	
	0.49	11.7	
	0.98	10.8	
	1.49	9.9	
	1.99	9.4	
Cu-DBC	2.48	8.9	*Angew. Chem.,Int. Ed.* **2020**, *59, 1081.*
	3.01	8.6	
	3.52	8.3	

		4.05	8.1	
		4.39	7.8	
		5.01	7.6	
Ni-HAB		0.021	14.8	*Nat. Energy.* **2018**, *3, 30.*
		0.052	14.3	
		0.099	13.8	
		0.187	13	
		0.419	11.6	
		0.73	10.1	
		1.21	8.4	
		2.175	6	
		3.05	4.2	
Cu-CAT NWAs		0.2	2.6	*Adv. Funct. Mater. 2017, 27, 1702067*
AC		12	6	*ACS Nano, 2013, 7, 5131.*
Commercial Supercapacitors	BCAP3000	5.294	4.0	*J. Power Sources 2000, 91, 37.*
	BCAP0310	3.846	3.1	
	Saft Gen2	3.125	6.0	
	Saft Gen3	6.923	6.8	
	Panasonic 800F	3.505	3.1	
	Superfarad 250 F	1.953	5.4	

Section 16. Atomic Coordinates of Cu-TBC

Table S9. Atomic coordinates of the AA-stacking model of Cu-TBC using Forcite method.

| | | **Space group: *P6*** | |
| | | | |

a = 20.1845 Å, b = 20.1845 Å, and c = 3.3200 Å.
$\alpha = \beta = 90°$, and $\gamma = 120°$

	X	**Y**	**Z**
C1	0.26372	0.66709	0.00475
C2	0.26369	0.59667	-0.00763
C3	0.47321	0.66728	-0.04428
C4	0.46836	0.59611	-0.07923
C5	0.40378	0.53146	0.07304
C6	0.33258	0.52669	0.04109
C7	0.26306	0.80733	-0.01232
C8	0.19287	0.73721	0.01173
C9	0.12376	0.73941	-0.01814
C10	0.12387	0.80835	-0.01354
C11	0.1923	0.87663	0.01873
C12	0.26111	0.87652	0.02117
O13	0.41267	0.479	0.22886
O14	0.52073	0.58735	-0.2374
H15	0.07186	0.69151	0.94433
H16	0.07341	0.80873	0.97031
H17	0.19218	0.93007	1.03895
H18	0.31153	0.93139	1.06466
Cu19	1	1.5	0.99521

Section 17. Supporting References

[S1] Z. Li, Z. Hu, X. Chen, Y. Zhang and J. Zhang, *Chem. Lett.*, 2012, **41**, 1588-1590.

[S2] J. Park, A. C. Hinckley, Z. Huang, D. Feng, A. A. Yakovenko, M. Lee, S. Chen, X. Zou and Z. Bao, *J. Am. Chem. Soc.*, 2018, **140**, 14533-14537

[S3] R. Matheu, E. Gutierrez-Puebla, M. Á. Monge, C. S. Diercks, J. Kang, M. S. Prévot, X. Pei, N. Hanikel, B. Zhang, P. Yang and O. M. Yaghi, *J. Am. Chem. Soc.*, 2019, **141**, 17081-17085

[S4] J. J. Liu, Y. Zhou, Z. Xie, Y. Li, Y. P. Liu, J. Sun, Y. H. Ma, O. Terasaki and L. Chen. *Angew. Chem. Int. Ed.,* 2020, **59**, 1081-1086.